NASA/CR- -97 208109 NIST-14695 NIS IN-71-CR (CUNY)

Journal of Engineering Mathematics **32:** 217–236, 1997.
© 1997 *Kluwer Academic Publishers. Printed in the Netherlands.*

On the computation of sound by large-eddy simulations

UGO PIOMELLI[1], CRAIG L. STREETT[2] and SUTANU SARKAR[3]
[1]*Department of Mechanical Engineering, University of Maryland, College Park, MD 20742, USA, e-mail: ugo@barolo.umd.edu*
[2]*NASA Langley Research Center, Hampton, VA 23681, USA*
[3]*Department of Applied Mechanics and Engineering Science, University of California at San Diego, La Jolla, CA 92093, USA*

Received 8 November 1996; accepted in revised form 14 February 1997

Abstract. The effect of the small scales on the source term in Lighthill's acoustic analogy is investigated, with the objective of determining the accuracy of large-eddy simulations when applied to studies of flow-generated sound. The distribution of the turbulent quadrupole is predicted accurately, if models that take into account the trace of the SGS stresses are used. Its spatial distribution is also correct, indicating that the low-wave-number (or frequency) part of the sound spectrum can be predicted well by LES. Filtering, however, removes the small-scale fluctuations that contribute significantly to the higher derivatives in space and time of Lighthill's stress tensor T_{ij}. The *rms* fluctuations of the filtered derivatives are substantially lower than those of the unfiltered quantities. The small scales, however, are not strongly correlated, and are not expected to contribute significantly to the far-field sound; separate modeling of the subgrid-scale density fluctuations might, however, be required in some configurations.

Key words: turbulent shear layers, large-eddy simulation, subgrid-scale models, acoustic analogy, Lighthill's analogy.

1. Introduction

Flow-generated noise is important in many engineering applications. It affects the observability and detection of aerial and submarine weapons systems, the comfort of passengers in airliners and automobiles, and may limit the operation of aircraft due to regulations that establish maximum levels of noise near airports. Furthermore, the interaction between sound and structures can have destructive effects.

An important source of noise is the sound generated by turbulence. This source was considered secondary in many applications (especially those involving aircraft, since the jet noise was usually dominant); however, the progress in jet-engine construction and design over recent years has been such that the airframe-noise problem is becoming more and more relevant.

Thus, there has been a considerable effort in recent years to study turbulent noise, to understand the mechanisms that lead to its generation, and, if possible, to control it. The numerical approach, in particular, has been the subject of significant research, because of the wealth of information that calculations can give compared to experiments, while requiring fewer, less restrictive, assumptions than theoretical studies.

The availability of powerful supercomputers has made possible the direct computation of sound, which involves the solution of the compressible Navier-Stokes (or Euler) equations to obtain both the near-field hydrodynamics and the far-field sound. Reviews of recent developments in computational techniques can be found in several references [1, 2, 3, 4]; here, we will only give some general considerations. The direct computation of sound requires no assumption, and provides multi-point information in the time (or frequency) domain. It is, thus, the

most general and powerful computational tool for aero-acoustic studies. It, however, suffers from significant limitations [4, 5]: it requires numerical schemes of high order of accuracy, reliable non-reflecting boundary conditions, and, most importantly, very large computational domains, given the disparity of scales between the aerodynamic and acoustic fields. For these reasons, the computational effort demanded by calculations of this kind is extreme, and only very simple cases have been attempted.

An approach that is more likely to be useful to study complex engineering applications is the acoustic analogy technique [6, 7], in which the aerodynamic and acoustic fields are decoupled. The near-field velocity and pressure are computed, and then used to calculate the far-field acoustic field, which is obtained from equations in which the aero- or hydrodynamic properties appear in a source term. This approach requires some simplifying assumptions: typically, two-way coupling is neglected, and the sound source (*i.e.*, the turbulent region of the flow) is required to be compact. It is, however, a technique that holds much promise of being an engineering tool, as long as relatively inexpensive ways of computing the velocity field can be found. Acoustic analogies have been used, in recent years, to study the sound emitted by homogeneous isotropic turbulence [8], jet noise [9], or the sound radiation during laminar breakdown [10]. A comparison between the direct computation of sound and the acoustic analogies was provided by Mitchell and co-authors [11], who confirmed the accuracy and validity of the acoustic analogy, as well as by Colonius and coworkers [3, 4].

Except for the jet-noise computations cited above [9], most of the calculations that use acoustic analogies have been carried out by direct numerical simulations (DNS), in which all scales of motion are resolved. However, since the computational cost of a DNS is proportional to the third power of the Reynolds number, it is unlikely that this technique can be applied successfully in the near future to engineering flows, *i.e.* at high Reynolds number and in complex geometries. Thus, the computation of the aerodynamic field by simpler, less computationally intensive methods, is desirable.

Two other techniques are available to obtain the velocity and pressure fields in turbulent flows: the solution of the Reynolds-averaged Navier-Stokes equations (RANS) and large-eddy simulation (LES). In the former, the governing equations are time- or phase-averaged; the dependent variables are then the ensemble-averaged velocity and pressure, and the effect of the turbulent fluctuations appears in the Reynolds-stress term which must represent the effect of all the scales of motion that have been removed in the averaging process. Several methods are available to parameterize the Reynolds stresses, ranging from simple, algebraic closures, to very complex, second-order models that require the solution of transport equations for each component of the Reynolds-stress tensor and for the viscous dissipation. This approach has two main limitations: first, the turbulence models tend to be not very general, since they are required to represent a disparate range of very different scales: coherent structures that are deterministic in nature, and depend strongly on the boundary conditions, and small eddies, more random and stochastic in character that can be more easily described in terms of statistical theories of turbulence. Furthermore, since RANS methods are based on phase- or time-averaging, they can only yield ensemble data, and most (or all) of the important information on the frequency content of the sound is lost.

The large-eddy simulation technique is a compromise between DNS and RANS: in LES the large, energy-carrying scales of motion are computed exactly, while only the small, subgrid scales are modeled. Since the latter depend essentially on the viscosity, and tend to be more homogeneous and isotropic than the coherent eddies, their effect on the large, resolved scales, which appears through the subgrid-scale (SGS) stress term, can be parameterized fairly

accurately by simple algebraic models. Since the evolution of the larger eddies is calculated accurately, LES can yield more accurate and complete results than RANS calculations, yet at a fraction of the cost of DNS. For these reasons, LES has become increasingly popular as a tool to study the physics of turbulent flows in configurations more complex than can be investigated by DNS. The development of a new generation of dynamic models [12, 13, 14], that allow the calculation of transitioning, relaminarizing and turbulent flows, while requiring few, if any, *ad hoc* adjustments, has made LES attractive for computations of technological relevance.

One issue that has not been addressed before, and that might affect the application of LES to sound computations, is the effect of the small scales on the source term in Lighthill's analogy. As mentioned above, in LES the smallest scales of motion disappear because of the averaging process, and their effect on the large scales is modeled. Mankbadi and co-workers [9] computed the sound directly from the resolved-scale velocity, assuming that the SGS field contribution to the sound source and the effect of the filtering operation were negligible. Although the contribution of the small scales to the momentum transport is usually small, their contribution to the sound generation may be more significant, in view of the fact that the source terms in the acoustic analogies involve derivatives of large-scale and SGS stresses, which are naturally more affected by the small scales.

This paper will deal with that particular issue, namely, the significance of the subgrid-scale contribution to the sound source, and its implications on the modeling of both the SGS stresses and the SGS density fluctuations. This objective will be achieved through an *a priori* analysis of the velocity fields obtained from the direct simulation of a turbulent flow. The velocity fields will be filtered, and the resolved and SGS contributions to the source will be computed. The source term calculated by means of the complete velocity will then be compared to that obtained from the resolved velocity (and modeled SGS stresses). The effects of filtering and order of accuracy of the differencing schemes will also be discussed.

In the next section, the mathematical formulation of the problem will be laid out, both for the LES governing equations and models, and for the acoustic analogy under consideration. Results will be presented and discussed in Section 3. Finally, conclusions will be drawn and recommendations for future work will be made in Section 4.

2. Problem formulation

2.1. Filtered equations of motion

In LES the resolved velocity and pressure are defined by the convolution of the original quantity with a filter function

$$\overline{f} = \int_{\mathcal{D}} f(\mathbf{x}')\, G(\mathbf{x} - \mathbf{x}')\, \mathrm{d}\mathbf{x}', \tag{1}$$

where the integral is extended over the entire computational domain $\mathcal{D}$, and $G(\mathbf{x} - \mathbf{x}')$ is the filter function, which determines the type of averaging performed to define the subgrid scales. Commonly used filters include the top-hat filter in real space

$$G(x) = \begin{cases} 1/\overline{\Delta} & \text{if } |x| \leqslant \overline{\Delta}/2 \\ 0 & \text{otherwise,} \end{cases} \tag{2}$$

the Gaussian

$$G(x) = \sqrt{\frac{6}{\pi\overline{\Delta}^2}} \exp\left(-\frac{6x^2}{\overline{\Delta}^2}\right) \tag{3}$$

and the Fourier cutoff filter, best defined in wave space[1]

$$\widehat{G}(k) = \begin{cases} 1 & \text{if } k \leqslant \pi/\Delta \\ 0 & \text{otherwise,} \end{cases} \tag{4}$$

where $\overline{\Delta}$ is the filter width, usually expressed in terms of the grid size Δx_i.

Applying the filtering operation (1) to the Navier–Stokes equations, we obtain the filtered Navier–Stokes equations, which, for an incompressible flow, take the form:

$$\frac{\partial \overline{u}_i}{\partial x_i} = 0, \tag{5}$$

$$\frac{\partial \overline{u}_i}{\partial t} + \frac{\partial}{\partial x_j}\left(\overline{u}_i \overline{u}_j\right) = -\frac{\partial \overline{p}}{\partial x_i} - \frac{\partial \tau_{ij}}{\partial x_j} + \nu \nabla^2 \overline{u}_i, \tag{6}$$

where $\tau_{ij} = \overline{u_i u_j} - \overline{u}_i \overline{u}_j$ are the SGS stresses, which must be modeled.

2.2. Lighthill's acoustic analogy

By combining the conservation of momentum with the time derivative of the mass-conservation equation, Lighthill [6] obtained the analogy that bears his name, which can be written as

$$\frac{\partial^2 \rho}{\partial t^2} - a_\infty^2 \nabla^2 \rho = \frac{\partial^2 T_{ij}}{\partial x_i \partial x_j}, \tag{7}$$

$$T_{ij} = \rho u_i u_j + \delta_{ij}(p - a_\infty^2 \rho) - \mu\left(\frac{\partial u_i}{\partial x_j} + \frac{\partial u_j}{\partial x_i}\right), \tag{8}$$

where a_∞ is the sound speed at free-stream (undisturbed) conditions. Lighthill's analogy (7–8) simplifies the coupled aerodynamic/acoustic problem to that of the propagation of sound in a fictitious acoustic medium at rest, on which the stress distribution T_{ij} is acting. Given T_{ij}, the pressure perturbation is given by

$$p - p_\infty = \frac{1}{4\pi} \int \frac{1}{r} \frac{\partial^2}{\partial x_i \partial x_j}\left[T_{ij}\left(\mathbf{y}, t - \frac{|\mathbf{x} - \mathbf{y}|}{a_\infty}\right)\right] \mathrm{d}\mathbf{y}, \tag{9}$$

where p_∞ is the ambient pressure. For points in the far field the integrand in (9) can be approximated by the second time derivative taken at the retarded time, yielding

$$p - p_\infty = \frac{1}{4\pi a_\infty^2} \frac{x_i x_j}{x^3} \int \frac{\partial^2}{\partial t^2}\left[T_{ij}\left(\mathbf{y}, t - \frac{|\mathbf{x} - \mathbf{y}|}{a_\infty}\right)\right] \mathrm{d}\mathbf{y}. \tag{10}$$

Lighthill's analogy is exact, but it requires that the stress distribution be known, and that it be zero in the region where the sound is calculated. If the DNS approach is used, the stress

tensor T_{ij} can be obtained from the velocity field. When LES or RANS are used, however, only the large-scale or ensemble-averaged parts of T_{ij} are available. They are given, respectively, by

$$\overline{T}_{ij} = \rho\overline{u}_i\overline{u}_j + \rho\tau_{ij} + \delta_{ij}(\overline{p} - a_\infty^2\rho) - \mu\left(\frac{\partial\overline{u}_i}{\partial x_j} + \frac{\partial\overline{u}_j}{\partial x_i}\right), \tag{11}$$

$$\langle T_{ij}\rangle = \rho\langle u_i u_j\rangle + \delta_{ij}(\langle p\rangle - a_\infty^2\langle\rho\rangle) - \mu\left(\frac{\partial\langle u_i\rangle}{\partial x_j} + \frac{\partial\langle u_j\rangle}{\partial x_i}\right), \tag{12}$$

where $\langle\cdot\rangle$ represents the ensemble average (time- or phase-average). Here and in the following, the flow is assumed to be incompressible.

A comparison of Equation (8) with (11) and (12) highlights the difference between the information that can be obtained with the three approaches: with DNS the entire spectral distribution of T_{ij} is known, and complete information (mean values, higher-order moments, and frequency spectra) can be obtained. On the other hand, the filtering operation implies that with LES only $\overline{T}_{ij}$, the low wave-number part of T_{ij}, is known. This includes the contribution of the nonlinear interactions between resolved ($\rho\overline{u}_i\overline{u}_j$) and subgrid scales ($\rho\tau_{ij}$) that result in resolved wave numbers; all interactions that generate wave numbers greater than the cutoff are lost because of the filtering operation. $\overline{T}_{ij}$ has the correct mean (since most filters are mean-preserving), but its higher moments are affected by the filtering operation, which, by its very nature, causes irretrievable loss of information. This is independent of the model chosen to parameterize the SGS stresses.

Similar considerations can be made regarding the source obtained from RANS, which, if time-averaging is used, contains no wave-number (or frequency) information at all; if phase-averaging is used, it may contain the frequency information due to the coherent structures that are preserved by the phase-averaging process only. The same considerations made above regarding the independence of this feature from the model used are valid here.

Thus, with reference to Figure 1, we can see that two sets of problems are raised by the filtering operation used in LES, and by the ensemble-averaging used in RANS: first is the fact that the unresolved part of T_{ij} may contribute substantially to the sound generation; it is important, therefore, to evaluate quantitatively its relevance. Secondly, it is useful to determine how accurately the SGS models (or, for RANS, the Reynolds-stress models) represent the contribution of the unresolved velocity scales to the resolved part of T_{ij}. These two problems are independent in the sense that improved modeling of the SGS or Reynolds stresses can only affect the second item, and an entirely different approach is required for the first problem, involving possibly separate modeling of the pressure (or density) fluctuations due to the unresolved part of T_{ij}.

2.3. *A PRIORI* TESTS

One method that is often used to study LES models and the physics of the large-scale/subgrid-scale interactions is the *a priori* test. This technique is based on the availability of velocity and pressure fields (usually from DNS), which are filtered to yield resolved and subgrid-scale fields. The *exact* SGS quantities can then be computed, as well as the predictions of SGS stress models. This method is inexpensive (if the DNS results are available), gives results that are not affected by numerical errors (since, typically the DNS calculations are performed on

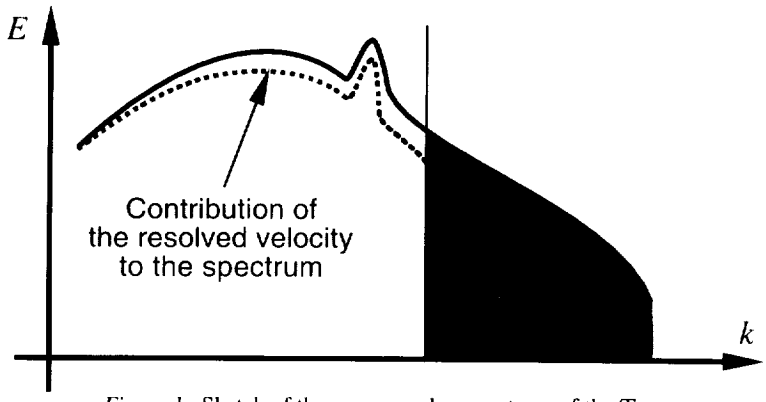

Figure 1. Sketch of the wave-number spectrum of the T_{ij}.

very fine grids with high order of accuracy), and allows to study the physical phenomena that affect the subgrid scales without any modeling assumption being required. Its disadvantages are that the Reynolds numbers are substantially lower than those of typical LES (since they are determined by the maximum Reynolds number achievable by the DNS), and that it is based on a frozen, instantaneous picture of the turbulence field that does not take into account the nonlinear dynamic interactions that take place between the resolved scales and the SGS model in an actual calculation.

In this work we have used the velocity fields obtained from the simulation of a plane channel flow, a classical test case for which very accurate and well-resolved DNS data is available. The present database is from a simulation of the flow at a Reynolds number (based on channel half-width, δ, and friction velocity, u_τ) $Re_\tau = 180$; $128\times97\times128$ grid points were used, and the governing equations were solved by a pseudo-spectral Fourier-Chebychev collocation method. The nonlinear terms were dealiased with the 3/2 rule. The results compared very well with experiments and other DNS calculations [15].

The velocity fields were filtered in the homogeneous directions by the top-hat (2) and cutoff (4) filters with widths varying between $\overline{\Delta}_i = 2\Delta x_i$ and $\overline{\Delta}_i = 4\Delta x_i$; these filter widths correspond to realistic situations, since the subgrid scales contain 15–25% of the turbulent kinetic energy with these widths (see [15]). Several schemes were used to compute the derivatives: second- and fourth-order differencing schemes, as well as high-order, spectral approximations.

The tensor T_{ij} and its filtered counterpart, $\overline{T}_{ij}$, were computed, as well as their second time derivatives $\partial^2 T_{ij}/\partial t^2$ and $\partial^2 \overline{T}_{ij}/\partial t^2$, which affect the far-field sound. The distribution of $\partial^2 T_{ij}/\partial x_i \partial x_j$ was also computed, together with its filtered counterpart.

3. Results and discussion

3.1. The stress field

Figure 2 shows the average of selected terms of the T_{ij} tensor. At low Mach numbers the pressure term is small, and will be neglected in this investigation. The main contribution comes from the resolved scales, the viscous stress being significant only in the near-wall region. The

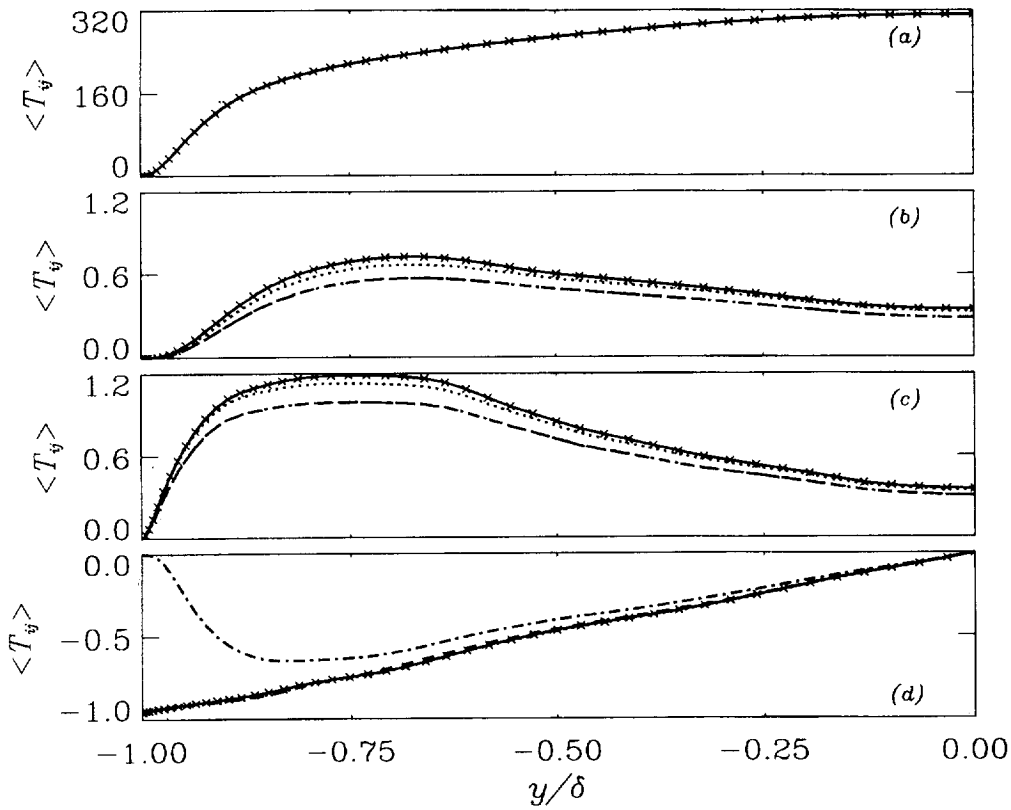

Figure 2. Average of T_{ij} and $\overline{T}_{ij}$. Top-hat filter, $\overline{\Delta}_i = 2\Delta x_i$; spectral differences. × T_{ij}, —·— $\overline{u}_i\overline{u}_j$ only, ——— $\overline{T}_{ij}$, exact SGS stresses; – – – $\overline{T}_{ij}$, dynamic model; ····· $\overline{T}_{ij}$, scale-similar model. (a) 11 component; (b) 22 component; (c) 33 component; (d) 12 component.

exact SGS stresses are compared with the prediction of two models: one is the dynamic model [12], an eddy-viscosity model of the form

$$\tau_{ij}^a = \tau_{ij} - \frac{\delta_{ij}}{3}\tau_{kk} = -2\nu_T\overline{S}_{ij} = -2C\overline{\Delta}^2|\overline{S}|\overline{S}_{ij}, \tag{13}$$

where

$$\overline{S}_{ij} = \frac{1}{2}\left(\frac{\partial\overline{u}_i}{\partial x_j} + \frac{\partial\overline{u}_j}{\partial x_i}\right) \tag{14}$$

is the resolved strain-rate tensor, and the model coefficient, C, is determined by means of the contraction proposed by Lilly [16]

$$C = -\frac{1}{2}\frac{\langle L_{ij}M_{ij}\rangle}{\langle M_{mn}M_{mn}\rangle}, \tag{15}$$

where $L_{ij} = \widehat{\overline{u}_i\overline{u}_j} - \widehat{\overline{u}}_i\widehat{\overline{u}}_j$ are the resolved turbulent stresses, $M_{ij} = \widehat{\overline{\Delta}}^2|\widehat{\overline{S}}|\widehat{\overline{S}}_{ij} - \overline{\Delta}^2\widehat{|\overline{S}|\overline{S}}_{ij}$, the application of a filter with width $\widehat{\overline{\Delta}} = 2\overline{\Delta}$ is denoted by $\widehat{\cdot}$, and $\langle\cdot\rangle$ represents averaging over a

plane parallel to the wall. The second is the scale-similar model proposed by Liu, Meneveau and Katz [17], which parameterizes the SGS stresses as $\tau_{ij} = 0{\cdot}45L_{ij}$.

Figure 2 shows that with LES the mean value of the tensor T_{ij} can be computed quite accurately. The behaviour of the T_{11} term is due to the fact that the mean velocity U was not removed during the computation of $\rho u_i u_j$. The largest discrepancies are observed in the 22 and 33 terms, and they are due to the eddy-viscosity assumption used to parameterize the subgrid scales, which allows to model only the anisotropic part of the SGS stress tensor; the contribution of the SGS stress-tensor trace, $\tau_{kk}/3$, is particularly significant near the wall and in the buffer layer, where the 11 term is dominant. Eddy-viscosity models cannot predict accurately the mean value of the the normal elements of the T_{ij} tensor unless the trace of the SGS stress tensor is determined. We can accomplish this in two ways: either by solving an additional equation for τ_{kk}, or by using a scale-similar or mixed model of the type proposed by Bardina *et al.* [18] or by Liu and coworkers [17]. Inclusion of the scale-similar part, in fact, gives improved prediction of the normal terms of T_{ij} (the dotted lines in Figure 2).

The *rms* of the same terms is shown in Figure 3, which highlights the effect of filtering: the *rms* of $\overline{T}_{ij}$ is lower than that of T_{ij} by 10–15%. Since the SGS stresses have very low (for this filter width) *rms* amplitude, the effect of the model is insignificant, and the sum of the resolved contribution and modeled SGS stresses agrees with the sum of resolved and exact SGS contributions.

Contours of the 11 and 22 components of the tensor T_{ij}, at $y^+ = (1 - |y|)u_\tau/\nu = 12$, are shown in Figures 4 and 5. The low-speed streaks characteristic of the near-wall region are evident in Figure 4. Both components show similar behaviours: $\overline{T}_{ij}$ is smoother than the T_{ij} field, but the location of strong events is captured very well, although at somewhat lower intensity (notice in particular the region highlighted in Figure 5). Both the dynamic eddy-viscosity and the scale-similar model reproduce this behaviour quite accurately. Similar results were obtained for all components of the T_{ij} tensor, throughout the channel. Figure 6, for instance, shows the T_{12} component at a location ($y^+ = 70$) in the logarithmic layer. The scale of the turbulent eddies at this distance from the wall is larger, but some difference can still be observed between the unfiltered and filtered fields.

The correct prediction of the spatial distribution of T_{ij} by LES is important for the correct prediction of the frequency content of the emitted sound, which can be related, through Taylor's hypothesis [19], to the wave-number spectrum of the sound source. If the spatial distribution and scale of the quadrupoles are predicted correctly, so will be the wave-number spectrum. If Taylor's hypothesis is valid (and numerical studies [20] indicate that, in the buffer region and beyond, such is indeed the case), an accurate prediction of the spatial distribution of the quadrupoles should, therefore, result in at least qualitatively accurate predictions of the low-frequency content of the sound radiated.

3.2. THE FAR FIELD

The sound in the far field can be obtained from (10). It may be useful, therefore, to compare the second derivatives of the quadrupole strength, $\ddot{T}_{ij} = \partial^2 T_{ij}/\partial t^2$ and $\ddot{\overline{T}}_{ij} = \partial^2 \overline{T}_{ij}/\partial t^2$. Numerically, the time derivatives are typically obtained by second-order-accurate central differences. Since most time-advancement schemes are also second-order-accurate, higher-order approximations do not give improved accuracy. Although DNS and LES calculations are, in general, over-resolved in time, since the CFL condition that determines the maximum time-step allowable restricts the maximum time-step allowable to values significantly larger than

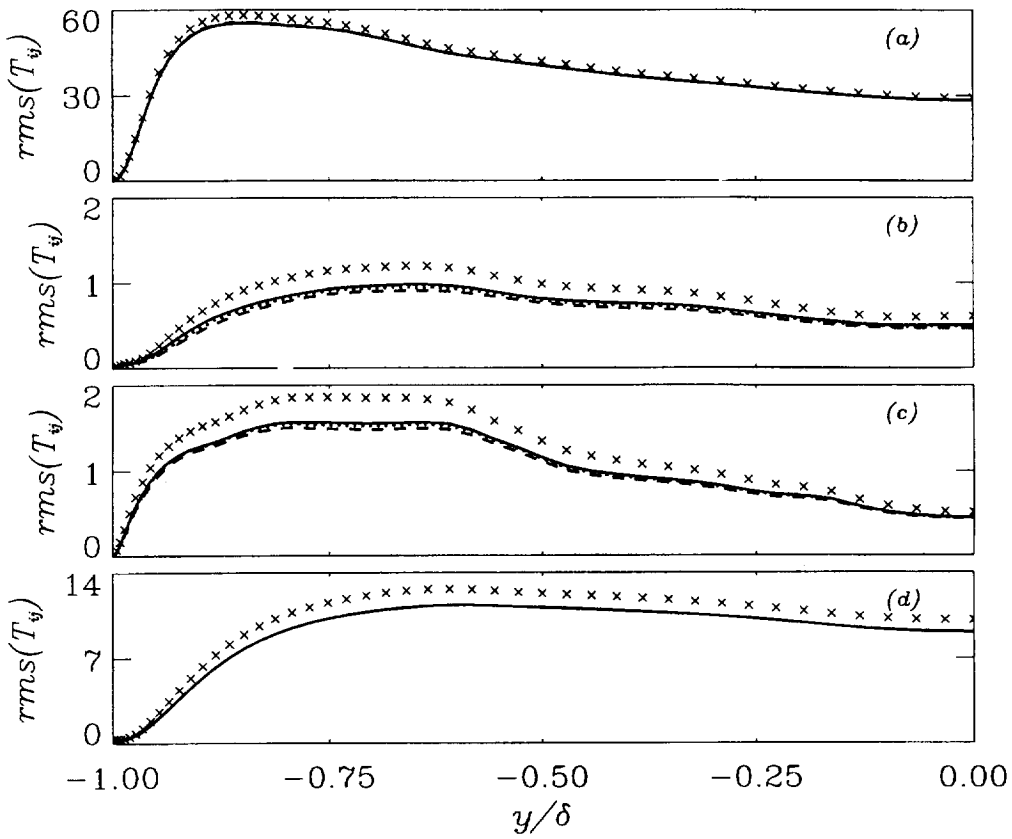

Figure 3. Root-mean-square (*rms*) fluctuations of T_{ij} and $\overline{T}_{ij}$. Top-hat filter, $\overline{\Delta}_i = 2\Delta x_i$; spectral differences. × T_{ij}, — · — $\overline{u}_i\overline{u}_j$ only, ——— $\overline{T}_{ij}$, exact SGS stresses; - - - $\overline{T}_{ij}$, dynamic model; ····· $\overline{T}_{ij}$, scale-similar model. (a) 11 component; (b) 22 component; (c) 33 component; (d) 12 component.

the time-scale of the smallest eddies in the flow, the additional filtering operation introduced by the second-order operator can have significant effects on the high-frequency structures. The numerical differentiation may introduce errors through an additional temporal filtering: if the second derivative of a complex exponential is calculated numerically, we will obtain

$$\frac{\delta^2}{\delta t^2} e^{i\omega t} = -\omega'^2 e^{i\omega t}, \tag{16}$$

where ω' is the modified frequency, and, for the central second-order accurate operator, it is equal to $\omega \sin(\omega\Delta t)/(\omega\Delta t)$. The amplitude of the second derivative of rapidly oscillating functions will thus be reduced substantially: even for structures whose characteristic period is equal to eight time-steps, the amplitude of the second derivative will be 80% of its true value.

Furthermore, the second derivative of a function is affected significantly by the short-lived small, whose wave-length is near the grid cutoff, which are the structures most likely to affect the higher derivatives. Since these structures are removed by the filtering operation, another source of error is introduced in the calculation of $\ddot{\overline{T}}_{ij}$.

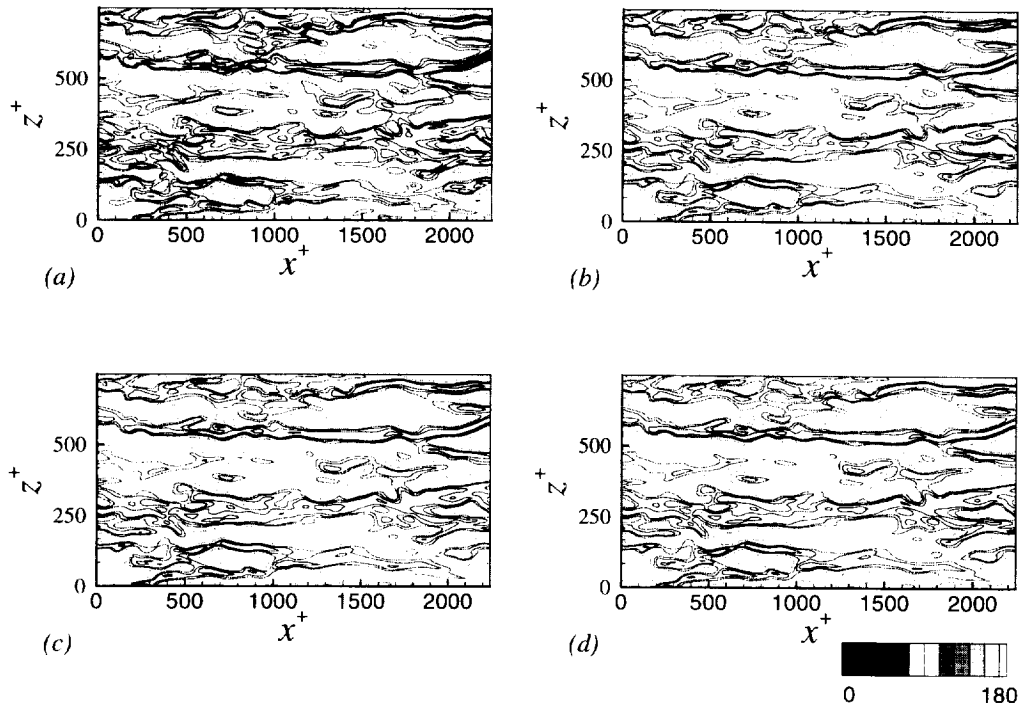

Figure 4. Contours of T_{11} at $y^+ = 12$. Top-hat filter, $\overline{\Delta}_i = 2\Delta x_i$, spectral differences. (a) T_{ij}; (b) $\overline{T}_{ij}$, exact SGS stresses; (c) $\overline{T}_{ij}$, dynamic model; (d) $\overline{T}_{ij}$, scale-similar model.

Figure 7, in which the *rms* of several terms of the tensor $\ddot{T}_{ij}$ are shown, illustrates these effects. We computed the second derivatives using two different time-steps, one equal to the time-step of the DNS, and one that was twice as large, more typical of LES calculations in which the grid size is coarser, and the CFL limitation is relaxed. The two results, respectively the solid and dashed lines in the figure, are nearly indistinguishable. The fact that, even if a small time-step is used, the *rms* of $\ddot{\overline{T}}_{ij}$ is 60% lower than that of $\ddot{T}_{ij}$ indicates that the temporal filtering does not remove additional scales over the spatial one, which is the most significant. While the *rms* and spatial distribution of T_{ij} are not affected very much by the filtering, the *rms* of $\ddot{T}_{ij}$ is. This is due to the fact that the small structures, as they are convected past an Eulerian point, cause a rapid change of T_{ij} in time, an effect that is amplified when second derivatives are taken. The removal of those small scales by the spatial filtering operation inhibits the accurate calculation of the high-frequency part of $\ddot{T}_{ij}$.

It should be remarked that the small eddies removed by the filtering operations are not strongly correlated, and their contributions to the sound are likely to cancel out in the far field. The contribution of the coherent eddies to $\ddot{\overline{T}}_{ij}$ is still captured quite accurately, as shown in Figures 8 and 9, in which contours of the $\ddot{T}_{11}$ and $\ddot{T}_{12}$ components are shown. The spatial distribution of the regions of significant $\ddot{T}_{ij}$ is predicted correctly, and the large-scale part appears well-captured. Only the contribution of the smallest scales is not present in the filtered $\ddot{\overline{T}}_{ij}$.

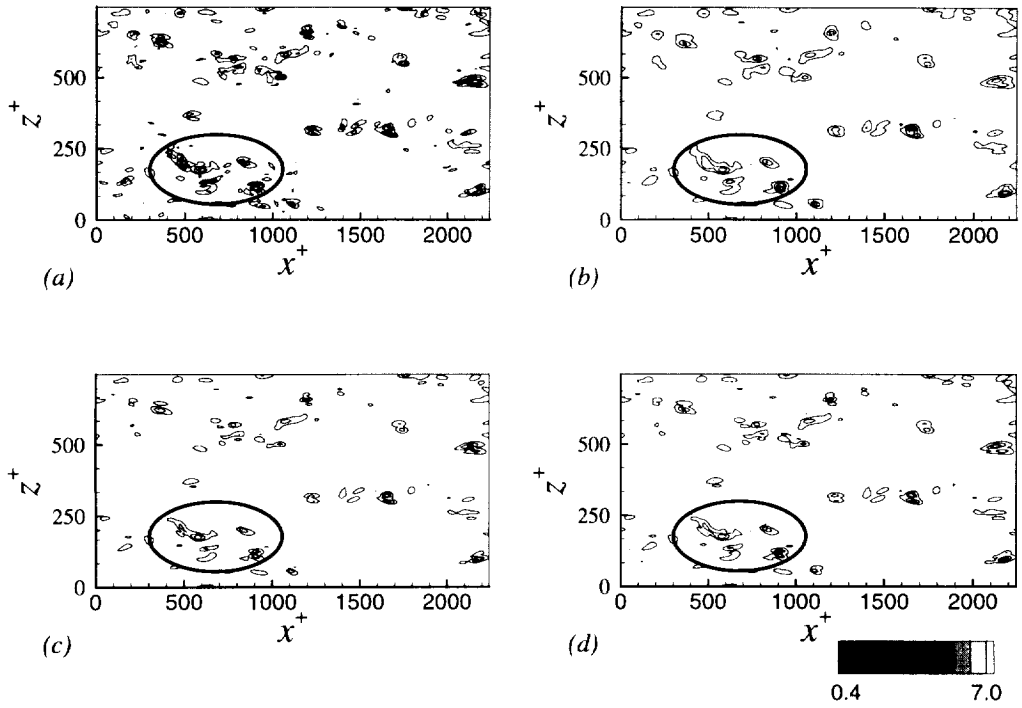

Figure 5. Contours of T_{22} at $y^+ = 12$. Top-hat filter, $\overline{\Delta}_i = 2\Delta x_i$, spectral differences. (a) T_{ij}; (b) $\overline{T}_{ij}$, exact SGS stresses; (c) $\overline{T}_{ij}$, dynamic model; (d) $\overline{T}_{ij}$, scale-similar model.

3.3. THE NEAR FIELD

As mentioned before, the expressions (9) and (10) are equivalent at far-field locations. The quantity $\partial^2 T_{ij}/\partial x_i \partial x_j$ is, however, much more difficult to compute than T_{ij} itself, being dominated by small-scale structures. In fact, to compute it accurately, it is necessary to resolve the entire dissipation spectrum. If, as is common in many DNS calculations, the spectra of the Reynolds stresses exhibit two to three orders of magnitude of decay, the Fourier coefficients of $\partial^2 T_{ij}/\partial x_i \partial x_j$, which are proportional to the wave-number squared multiplied by the Fourier coefficients of T_{ij}, do not decay appreciably over the range of the resolved wave numbers and their spectrum is nearly flat. Thus, we would expect numerical errors and filtering to have a significant effect. Furthermore, since the sound is due to the small amount of disturbance left after the cancellation of the contribution to the sound of the positive and negative values that are generated by the repeated differentiation, use of (9) to evaluate the far-field sound is not advisable. Regardless of these *caveats*, an examination of the behaviour of $\partial^2 T_{ij}/\partial x_i \partial x_j$ may at least give some bound on the accuracy that can be expected from LES and DNS calculations, especially for the computation of the sound in the near-field, where (9) and (10) are not equivalent.

Figure 10 shows the mean and *rms* profiles of $\partial^2 T_{ij}/\partial x_i \partial x_j$. In plane channel flow, the only term that contributes to the average value is the 22 term. Since $\langle v \rangle = 0$ in parallel flow, the viscous contribution vanishes, and the total and filtered contributions can be written as

$$\frac{\partial^2 \langle T_{ij} \rangle}{\partial x_i \partial x_j} = \frac{\partial^2}{\partial y^2} \left(\rho \langle v v \rangle \right); \qquad \frac{\partial^2 \langle \overline{T}_{ij} \rangle}{\partial x_i \partial x_j} = \frac{\partial^2}{\partial y^2} \left(\rho \langle \overline{v}\, \overline{v} \rangle + \rho \langle \tau_{22} \rangle \right). \tag{17}$$

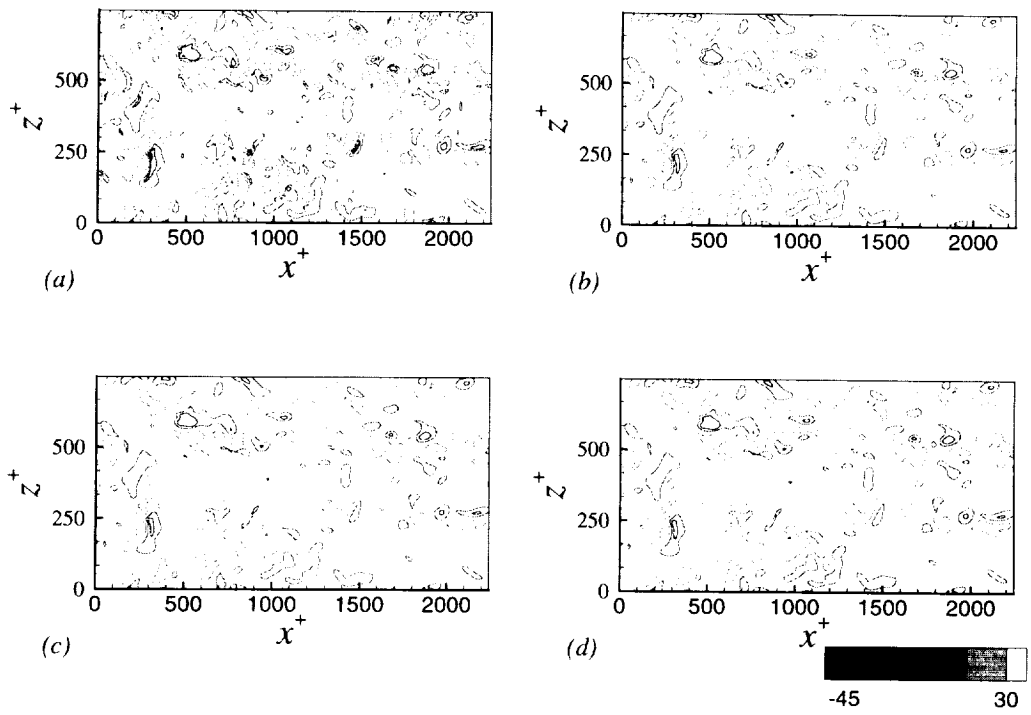

Figure 6. Contours of T_{12} at $y^+ = 70$. Top-hat filter, $\overline{\Delta}_i = 2\Delta x_i$, spectral differences. (a) T_{ij}; (b) $\overline{T}_{ij}$, exact SGS stresses; (c) $\overline{T}_{ij}$, dynamic model; (d) $\overline{T}_{ij}$, scale-similar model.

If the exact SGS stresses are used, these two quantities are identical, since the filter is mean-preserving. The difference between this value and the value of $\partial^2\overline{T}_{ij}/\partial x_i\partial x_j$ obtained with the dynamic model is again due to the eddy-viscosity assumption used to parameterize the subgrid scales; use of the scale-similar model gives improved results.

The normal components of the SGS stress tensor affect the mean of $\partial^2 T_{ij}/\partial x_i\partial x_j$ more than its *rms* value. Figure 10b compares the *rms* profiles of $\partial^2 T_{ij}/\partial x_i\partial x_j$ with those of $\partial^2\overline{T}_{ij}/\partial x_i\partial x_j$. A significant difference can be observed between the unfiltered and filtered values of this quantity, a difference not due to modeling errors, but purely to the filtering operation, which removes the high-wave-number (and frequency) components of the velocity field that affect the higher derivatives of T_{ij} more than they affect T_{ij} itself. This difference is of the same order as the difference between the *rms* of $\ddot{T}_{ij}$ and $\ddot{\overline{T}}_{ij}$ observed before.

The difference between the *rms* values of $\partial^2\overline{T}_{ij}/\partial x_i\partial x_j$ we obtained using the exact and the modeled SGS stresses, is small. While the wall-normal component of T_{ij} determines the mean value of the strength of the quadrupoles, its fluctuations are mostly affected by the shear components, which are typically predicted more accurately than the normal ones by the SGS model.

To determine whether the filtering procedure alters the wave-number (or frequency) spectra of $\partial^2 T_{ij}/\partial x_i\partial x_j$ in Figure 11 the contours of the unfiltered and filtered quantities are shown in a plane parallel to the wall at $y^+ = 12$. The locations at which large-magnitude regions of $\partial^2 T_{ij}/\partial x_i\partial x_j$ and $\partial^2\overline{T}_{ij}/\partial x_i\partial x_j$ occur are fairly well-correlated, although regions of significant strength are, of course, less sharp after the filtering.

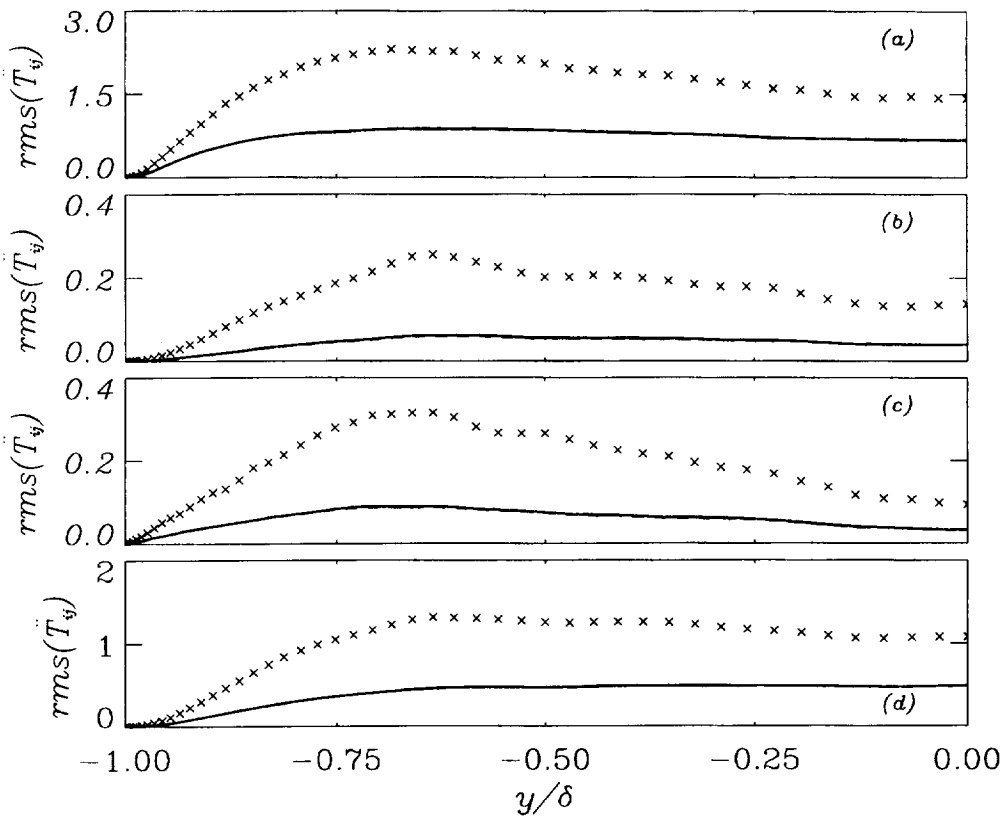

Figure 7. Root-mean-square (*rms*) fluctuations of $\ddot{T}_{ij}$ and $\overline{\ddot{T}}_{ij}$. Top-hat filter, $\overline{\Delta}_i = 2\Delta x_i$; spectral differences. $\times$ T_{ij}; ——— $\overline{T}_{ij}$, exact SGS stresses, $\Delta t_{LES} = \Delta t_{DNS}$; - - - $\overline{T}_{ij}$, exact SGS stresses, $\Delta t_{LES} = 2\Delta t_{DNS}$. (a) 11 component; (b) 22 component; (c) 33 component; (d) 12 component.

This correspondence is due to the fact that the regions in which $\partial^2 \overline{T}_{ij}/\partial x_i \partial x_j$ has significant magnitude are fairly well correlated with energy-producing events (which are well-predicted by the LES) in the buffer region: Figure 12 compares the contours of $\partial^2 T_{ij}/\partial x_i \partial x_j$ and $\overline{\ddot{T}}_{ij}$ with those of T_{11} and T_{12} (representative, respectively, of the low-speed streaks and the principal shear component of the Reynolds stress tensor). Strong correlation between the Reynolds stresses and $\partial^2 \overline{T}_{ij}/\partial x_i \partial x_j$ can be observed at several locations (some of them highlighted in the figure).

3.4. Effect of filter width and differencing scheme

Some remarks should be made about the effects of the filter width and the differencing scheme used. When the cutoff filter with width $\overline{\Delta}_i = 4\Delta x_i$ was used, results similar to those presented here were obtained. If a top-hat filter with width $\overline{\Delta}_i = 4\Delta x_i$ was applied, however, the *rms* of $\partial^2 \bar{T}_{ij}/\partial x_i \partial x_j$ decreased further (Figure 13), reflecting the fact that the subgrid scales contain an excessive amount of energy to ensure an accurate calculation. The T_{ij} field is also substantially smoother (Figure 14).

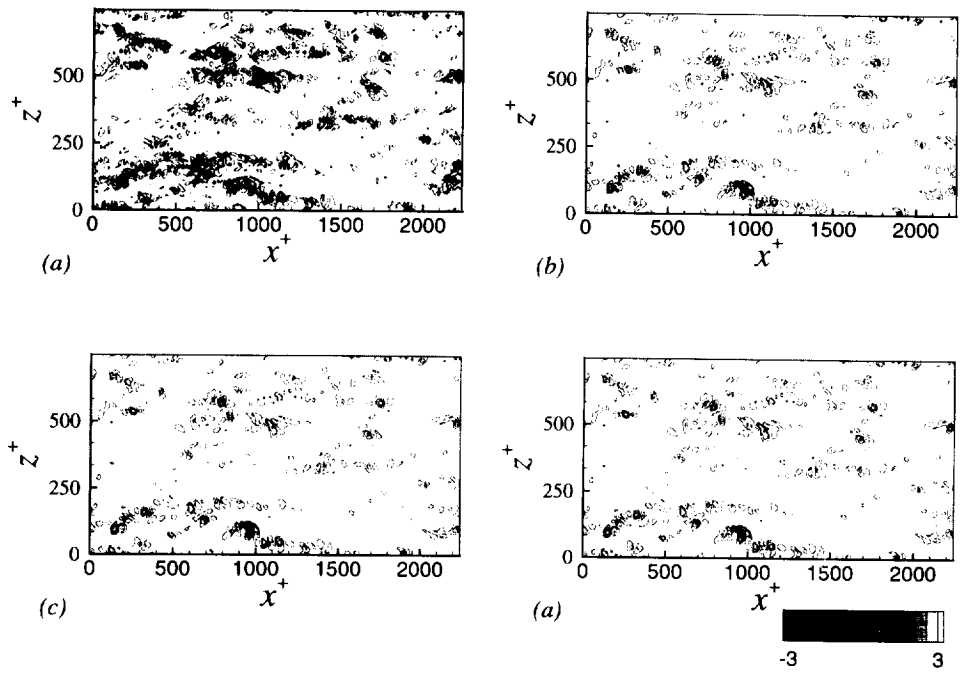

Figure 8. Contours of $\ddot{T}_{11}$ and $\ddot{\overline{T}}_{11}$ at $y^+ = 12$. Top-hat filter, $\overline{\Delta}_i = 2\Delta x_i$, spectral differences, $\Delta t_{LES} = 2\Delta t_{DNS}$. (a) $\ddot{T}_{ij}$; (b) $\ddot{\overline{T}}_{ij}$, exact SGS stresses; (c) $\ddot{\overline{T}}_{ij}$, dynamic model; (d) $\ddot{\overline{T}}_{ij}$, scale-similar model.

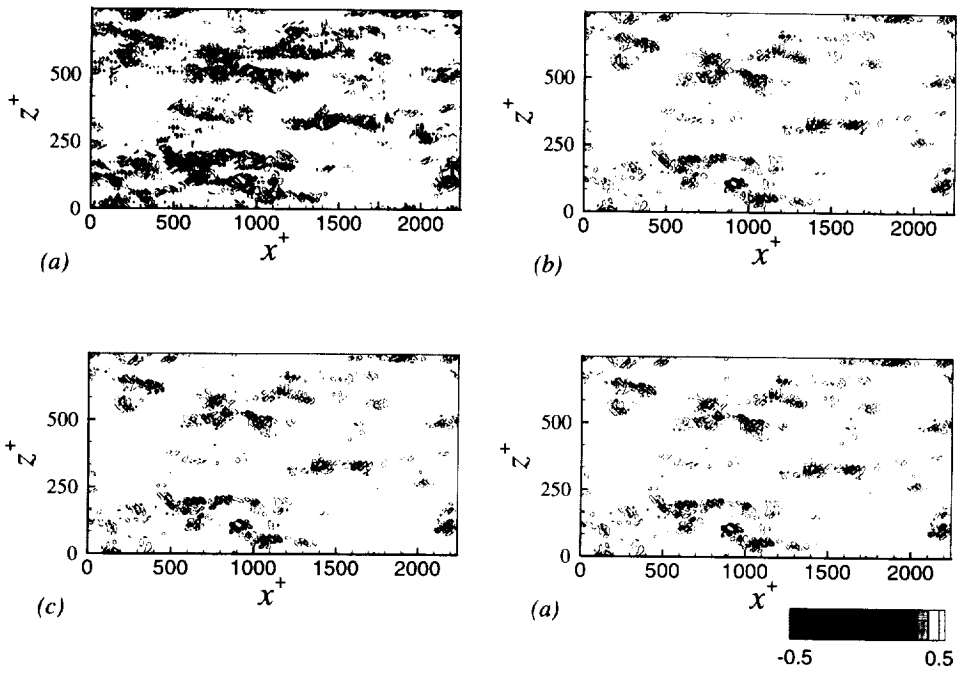

Figure 9. Contours of $\ddot{T}_{12}$ and $\ddot{\overline{T}}_{12}$ at $y^+ = 12$. Top-hat filter, $\overline{\Delta}_i = 2\Delta x_i$, spectral differences, $\Delta t_{LES} = 2\Delta t_{DNS}$. (a) $\ddot{T}_{ij}$; (b) $\ddot{\overline{T}}_{ij}$, exact SGS stresses; (c) $\ddot{\overline{T}}_{ij}$, dynamic model; (d) $\ddot{\overline{T}}_{ij}$, scale-similar model.

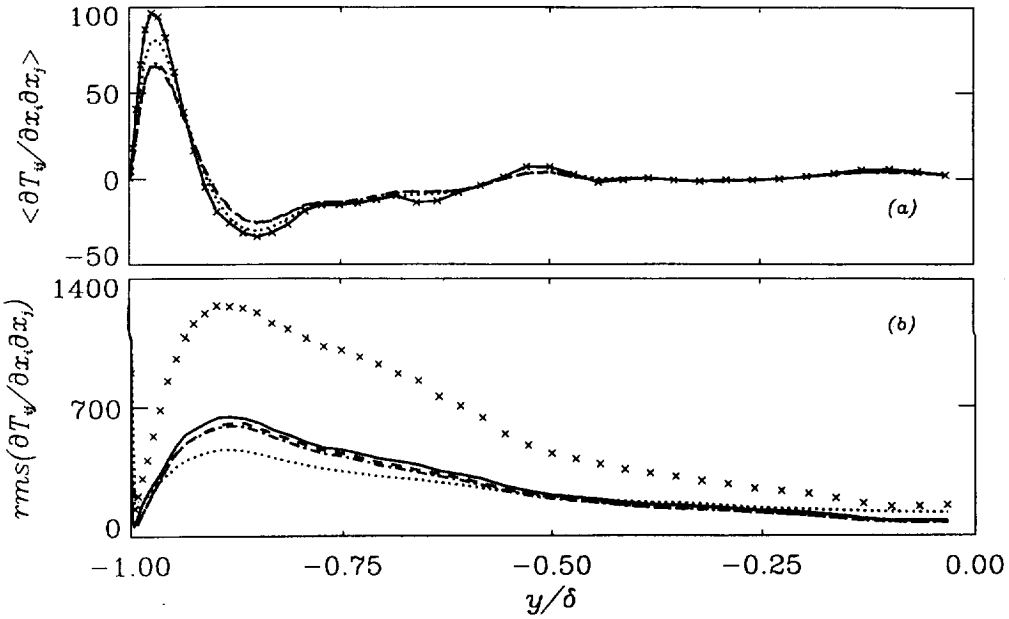

Figure 10. Average and *rms* values of $\partial^2 T_{ij}/\partial x_i \partial x_j$. Top-hat filter, $\overline{\Delta}_i = 2\Delta x_i$; spectral differences. × T_{ij}, —·— $\overline{u}_i\overline{u}_j$ only, ——— $\overline{T}_{ij}$, exact SGS stresses; – – – $\overline{T}_{ij}$, dynamic model; ····· $\overline{T}_{ij}$, scale-similar model. (a) Average; (b) *rms*.

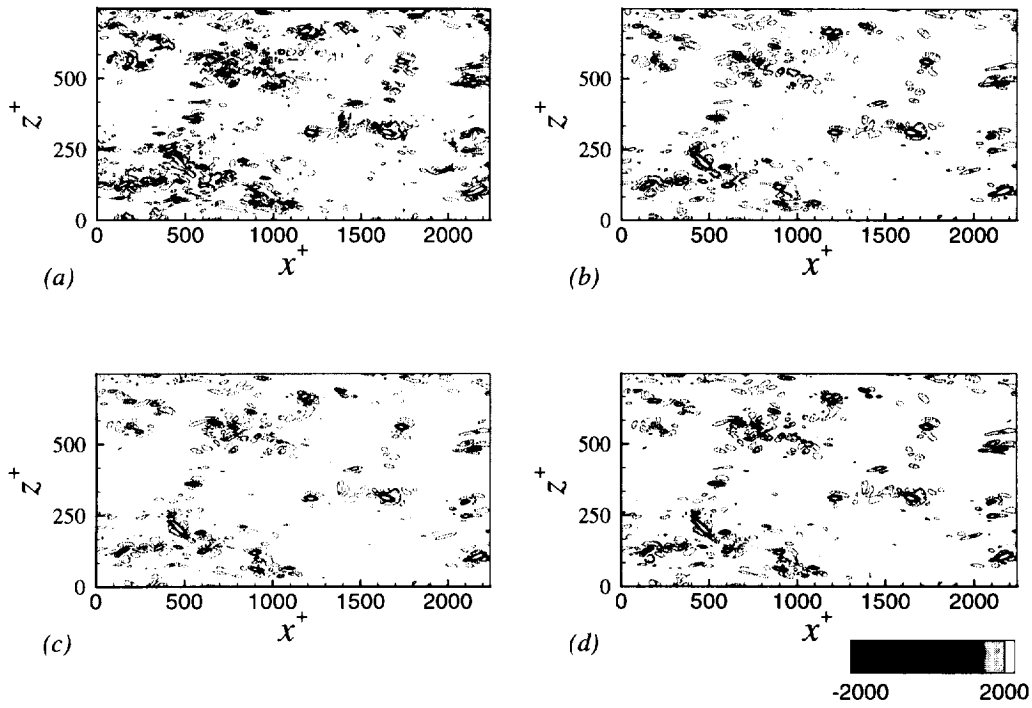

Figure 11. Contours of $\partial^2 T_{ij}/\partial x_i \partial x_j$ at $y^+ = 12$. Top-hat filter, $\overline{\Delta}_i = 2\Delta x_i$, spectral differences. (a) T_{ij}; (b) $\overline{T}_{ij}$, exact SGS stresses; (c) $\overline{T}_{ij}$, dynamic model; (d) $\overline{T}_{ij}$, scale-similar model.

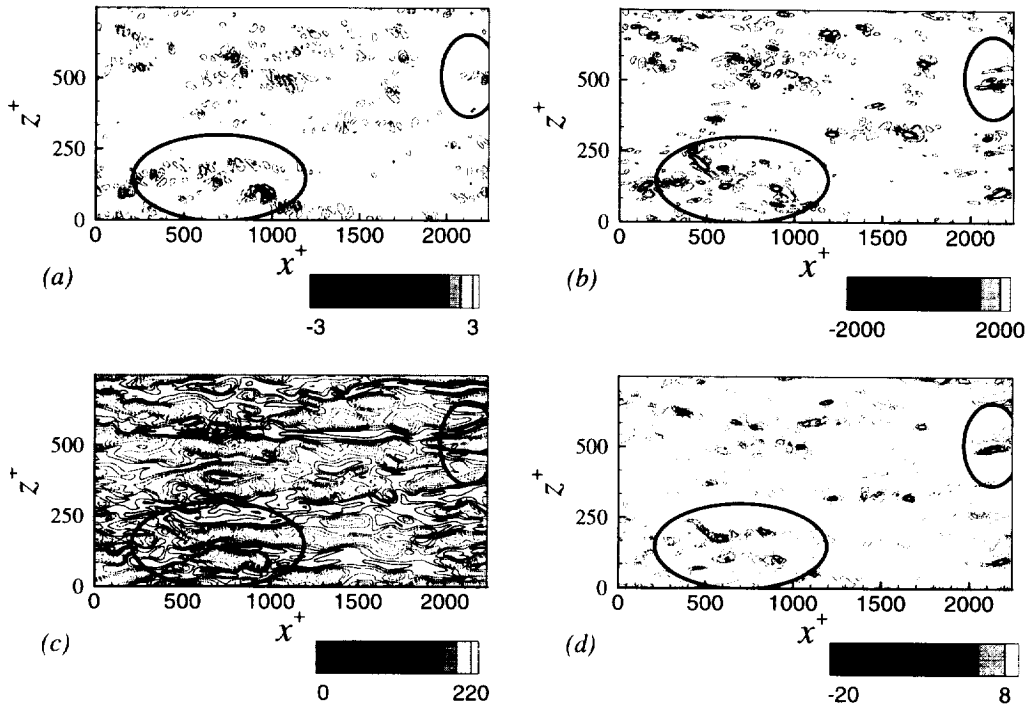

Figure 12. Contours of $\partial^2\overline{T}_{ij}/\partial x_i\partial x_j$, $\ddot{\overline{T}}_{ij}$, and T_{ij} at $y^+ = 12$. Top-hat filter, $\overline{\Delta}_i = 2\Delta x_i$, spectral differences. (a) $\ddot{\overline{T}}_{11}$; (b) $\partial^2\overline{T}_{ij}/\partial x_i\partial x_j$; (c) T_{11}; (d) T_{12}.

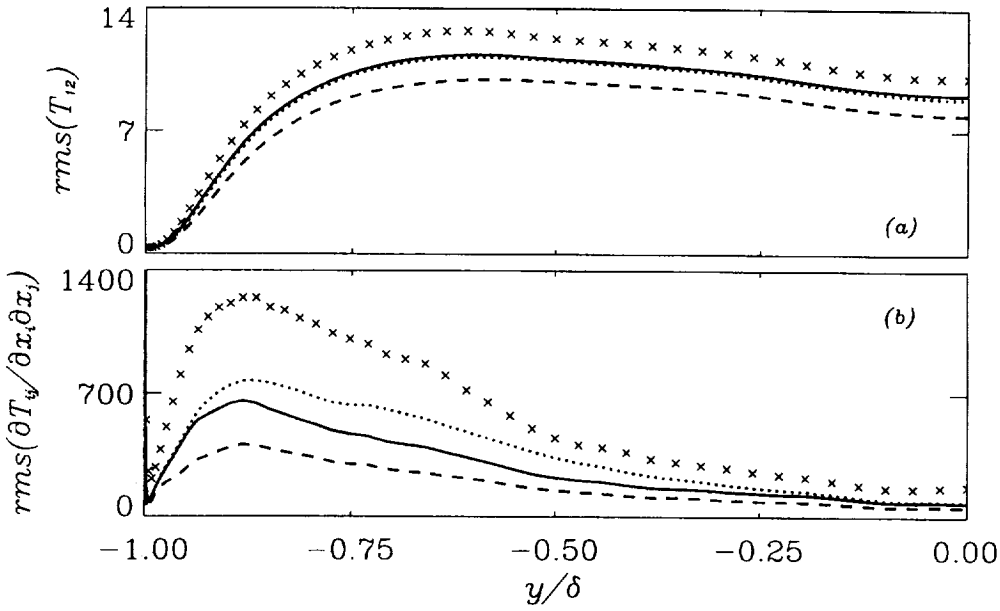

Figure 13. Root-mean-square (*rms*) fluctuations of $\overline{T}_{12}$ and $\partial^2\overline{T}_{ij}/\partial x_i\partial x_j$. Spectral differences. × Unfiltered, ——— top-hat, $\overline{\Delta}_i = 2\Delta x_i$; – – – top-hat, $\overline{\Delta}_i = 4\Delta x_i$; ····· cutoff, $\overline{\Delta}_i = 4\Delta x_i$. (a) $\overline{T}_{12}$; (b) $\partial^2\overline{T}_{ij}/\partial x_i\partial x_j$.

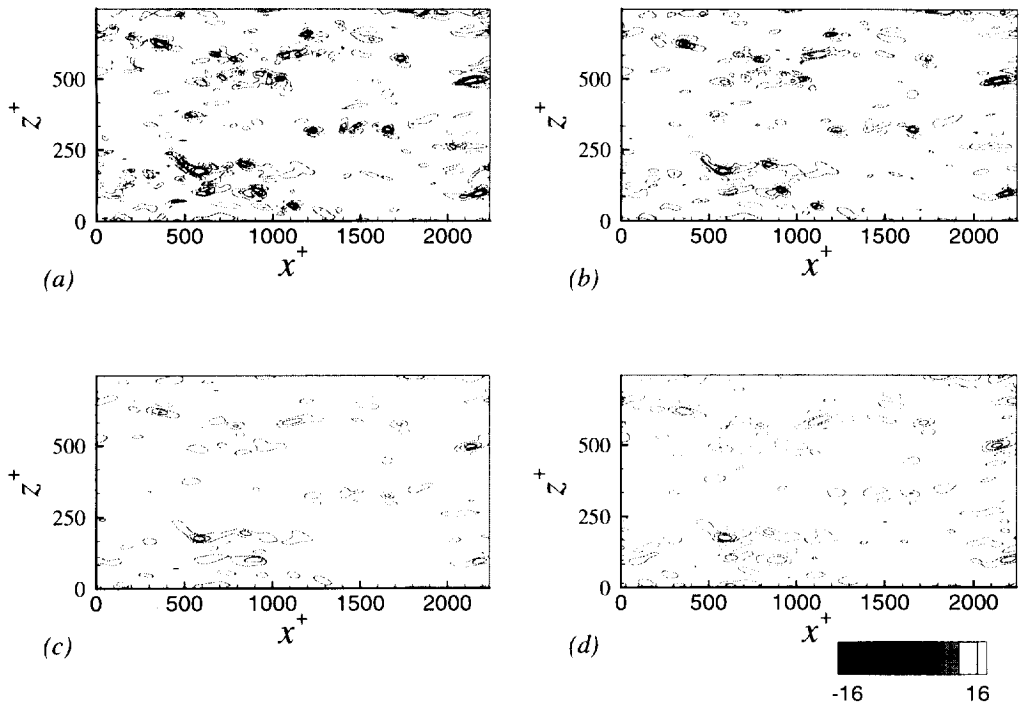

Figure 14. Contours of T_{12} at $y^+ = 12$. (a) Unfiltered; (b) ——— , top-hat, $\overline{\Delta}_i = 2\Delta x_i$; (c) ——— , top-hat, $\overline{\Delta}_i = 4\Delta x_i$; (d) ——— , cutoff, $\overline{\Delta}_i = 4\Delta x_i$.

Errors in the numerical evaluation of the second derivatives are significant only if the distribution of $\partial^2 T_{ij}/\partial x_i \partial x_j$ is desired: very little difference was observed in $\overline{T}_{ij}$, whether the SGS model was computed by spectral approximation or second-order differences. More significant were the differences between the $\partial^2 T_{ij}/\partial x_i \partial x_j$, which are illustrated in Figure 15. The peak values of $\partial^2 \overline{T}_{ij}/\partial x_i \partial x_j$ when the second-order differences and the coarser filter were used (Figure 15d) were three times smaller than those obtained with spectral differences and the finer filter.

4. Conclusions

An *a priori* study of the quadrupole distribution in Lighthill's analogy [6] has been carried out. The velocity fields obtained from well-resolved simulations of plane channel flow were filtered to yield resolved and subgrid-scale velocity components. These, in turn, were used to compute the tensor T_{ij} and its filtered counterpart $\overline{T}_{ij}$. The filtered and unfiltered values of $\partial^2 T_{ij}/\partial t^2$ and $\partial^2 T_{ij}/\partial x_i \partial x_j$ were also compared.

The mean value of the strength of the $\partial^2 T_{ij}/\partial x_i \partial x_j$ is evaluated accurately; it is, however, desirable to use models that include the trace of the SGS stress, which can give a significant contribution to the mean T_{22}. The *rms* of T_{ij}, on the other hand, is lower than the unfiltered one. Modeling the SGS stresses does not cause significant errors beyond those introduced by the filtering itself.

The results presented indicate that the spatial distribution of the source is affected mostly by the resolved scales. Thus, we should expect the wave-number distribution of the filtered

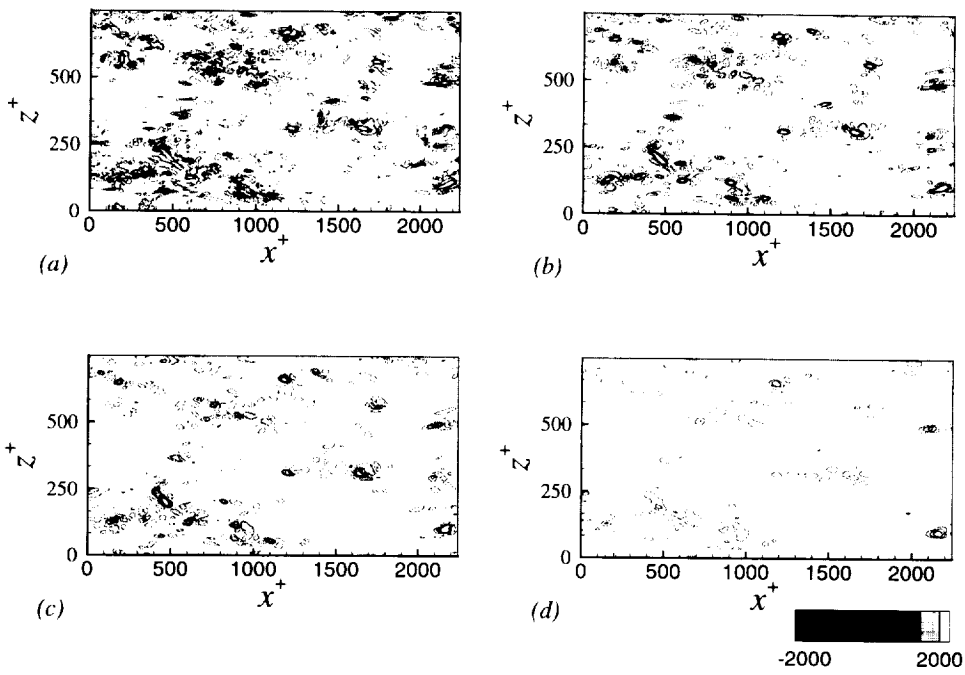

Figure 15. Contours of $\partial^2 T_{ij}/\partial x_i \partial x_j$ at $y^+ = 12$. (a) Unfiltered; (b) top-hat filter, $\overline{\Delta}_i = 2\Delta x_i$, spectral differences; (c) top-hat filter, $\overline{\Delta}_i = 2\Delta x_i$, second-order differences; (d) top-hat filter, $\overline{\Delta}_i = 4\Delta x_i$, second-order differences.

source to have the correct shape (*i.e.*, peaks at the correct wave-numbers) up to the cutoff wave-number. In conditions in which Taylor's hypothesis of frozen turbulence holds, it is possible to relate the wave-numbers to the frequencies through a convection velocity; an accurate prediction of the spatial distribution of the source should, therefore, result in at least qualitatively accurate predictions of the low-frequency content of the sound radiated.

The present investigation supplies criteria to evaluate the accuracy with which turbulent sound can be predicted by LES calculations. The contribution of the largest turbulent eddies (such as the hairpins present in a turbulent boundary layer) is predicted accurately, although some reduction of their amplitude is observed due to the filtering operation. SGS models that account for the trace of the SGS stresses are, however, required to obtain accurate prediction of the source. Based on the present results, it can be conjectured that the contribution of coherent structures (shed vortices, for instance) would also be captured accurately, resulting in satisfactory prediction of the low-wave-number part of the spectrum.

The high-wave-number components of the source, on the other hand, are removed by the filtering procedure, and cannot be recovered by more accurate SGS modeling. These components affect significantly the higher derivatives of T_{ij}, both with respect to time or space. This limitation is likely to affect similarly the RANS prediction. These small-scale fluctuations are largely uncorrelated, and are not expected to affect the far-field sound significantly, and in most cases (when coherent structures are present that account for the greatest part of sound generated, which are accurately computed) their accurate prediction might be of secondary importance. In other applications it might be necessary to derive a model for the unresolved

contribution to the sound intensity, ρ^2, which can be decomposed into a term, $\overline{\rho}^2$ due to the resolved source $\overline{T}_{ij}$, plus another due to the unresolved part, $\tau_\rho = \rho^2 - \overline{\rho}^2$.

A possible way to evaluate the SGS contribution to the sound intensity, τ_ρ, might be to consider the subgrid scales in a computational control volume (a grid cell) as a small volume of homogeneous isotropic turbulence. Turbulence theory can then be applied (see, for instance, [21, 7]) to estimate the sound emitted by the small volume of homogeneous isotropic turbulence, *i.e.*, the subgrid scales, subjected to the local shear and strain field given by the large-scale strain-rate tensor $\overline{S}_{ij}$. The development of this type of model can, conceivably, correct the computed sound pressure, and be a valuable contribution towards making LES a useful tool for the prediction of these type of problems.

Acknowledgments

The authors thank Sir James Lighthill for his constructive comments as a referee on the first version of this paper. This research was supported partly by the George Washington University through NASA Contract NAS 1-19699.

Note

[1] Unless otherwise noted, a quantity denoted by a caret $\widehat{\cdot}$ is the complex Fourier coefficient of the original quantity.

References

1. M. J. Lighthill, Report on the final panel discussion on computational aeroacoustics. *ICASE Report No. 92-53* (1992) 14 pp.
2. D. G. Crighton, Computational aeroacoustics for low Mach number flows. In: J. C. Hardin and M. Y. Hussaini (eds.) *Computational Aeroacoustics*. New York: Springer-Verlag (1993) pp. 50–68.
3. T. Colonius, P. Moin and S. Lele, Direct computation of aerodynamic sound. *Report TF-65* Thermosciences Division, Department of Mechanical Engineering, Stanford University (1995) 222 pp.
4. T. Colonius, *Direct Computation of Aerodynamic Sound*. Ph.D. Dissertation, Stanford University (1995), 212 pp.
5. T. Colonius, P. Moin and S. Lele, Boundary conditions for direct computation of aerodynamic sound. *AIAA J.* 31 (1993) 1574-1582.
6. M. J. Lighthill, On sound generated aerodynamically; I. General theory. *Proc. R. Soc. Lond. A* 211 (1952) 564–587.
7. M. J. Lighthill, On sound generated aerodynamically; II. Turbulence as a source of sound. *Proc. R. Soc. Lond. A* 222 (1952) 1–32.
8. S. Sarkar and M. Y. Hussaini, Computation of the acoustic radiation from bounded homogeneous flow. In: J. C. Hardin and M. Y. Hussaini (eds.) *Computational Aeroacoustics*. New York: Springer-Verlag (1993) pp. 335–355.
9. R. R. Mankbadi, M. E. Hayer, L. A. Povinelli, Structure of supersonic jet flow and its radiated sound. *AIAA J.* 5 (1994) 897–906.
10. M. Wang, S. Lele, and P. Moin, Sound radiation during local laminar breakdown in a low Mach-number boundary layer. *J. Fluid Mech.* 319 (1996) 197–218.
11. B. E. Mitchell, S. Lele, and P. Moin, Direct computation of sound from a compressible co-rotating vortex pair. *J. Fluid Mech.* 285 (1993) 181–202.
12. M. Germano, U. Piomelli, P. Moin, and W. H. Cabot, A dynamic subgrid-scale eddy viscosity model. *Phys. Fluids A* 3 (1991) 1760–1765.
13. S. Ghosal, T. S. Lund, P. Moin, and K. Akselvoll, A dynamic localization model for large-eddy simulation of turbulent flow. *J. Fluid Mech.* 286 (1995) 229–255.
14. U. Piomelli, and J. Liu, Large eddy simulation of rotating channel flows using a localized dynamic model. *Phys. Fluids* 3 (1995) 839–848.
15. U. Piomelli, Y. Yu, and R. J. Adrian, Subgrid-scale energy transfer and near-wall turbulence structure. *Phys. Fluids* 8 (1996) 215–224.

16. D. K. Lilly, A proposed modification of the Germano subgrid-scale closure method. *Phys. Fluids A* 4 (1992) 633–635.
17. S. Liu, C. Meneveau and J. Katz, On the properties of similarity subgrid–scale models as deduced from measurements in a turbulent jet. *J. Fluid Mech.* 275 (1994) 83–119.
18. J. Bardina, J. H. Ferziger and W. C. Reynolds, Improved subgrid scale models for large eddy simulation. *AIAA* Paper No. 80–1357 (1980) 9 pp.
19. G. I. Taylor, The spectrum of turbulence. *Proc. R. Soc. London A* 164 (1938) 476–000.
20. U. Piomelli, J.-L. Balint and J. M. Wallace, On the validity of Taylor's hypothesis for wall-bounded turbulent flows. *Phys. Fluids A* 1 (1989) 609–611.
21. I. Proudman, The generation of sound by isotropic turbulence *Proc. R. Soc. Lond. A* 214 (1952) 119–132.